Research Paper
Computational Methods for Differential Equations
http://cmde.tabrizu.ac.ir
Vol. *, No. *, *, pp. 1-18
DOI:10.22034/cmde.2025.66263.3086

Rotating Casson Nanofluid Flow with Generalized Heat and Mass Transport

Muhammad Samiullah, Muhammad Sagheer, and Hassan Shahzad*
Capital University of Science and Technology, Department of Mathematics, Islamabad, 44000, Pakistan.

Abstract

A theoretical investigation is conducted to explore the three-dimensional Casson nanofluid flow affected by the double diffusion effects in Casson nanofluid over a stretching sheet, considering viscous dissipation, thermal radiation, inclined magnetic field, porous medium, chemical reaction, and heat generation/absorption. The study addresses a research gap by incorporating the Cattaneo-Christov double diffusion model into the rotating Casson nanofluid framework, which has not been previously considered in such the three-dimensional flow. The inclusion of radiative heat and inclined magnetic field effects further enhances the novelty of the current work. Governing nonlinear partial differential equations are transformed into the ordinary differential equations using the similarity transformations and solved numerically via the shooting method. Key transport mechanisms such as thermophoresis, Brownian motion, and thermal and mass relaxation effects are analyzed. The results indicate that a 40% increase in the Casson parameter leads to a reduction in the heat transfer rate by up to 23%. An increased rotation and magnetic field strength also contribute to the reduced velocity and thermal profiles. This research provides a deeper understanding of non-Fourier heat and mass transport in non-Newtonian fluids. The findings are applicable to cooling technologies, polymer processing, and enhanced heat transfer systems involving electrically conducting fluids.

Keywords. Cattaneo-Christov double diffusion, Inclined MHD, Heat generation/absorption, Porous medium, Chemical reaction rate.
1991 Mathematics Subject Classification.

1. INTRODUCTION

The specific branch of fluid mechanics that focuses on describing the motion of fluids (gases/ liquids), is known as fluid dynamics. Aerodynamics and hydrodynamics are notable branches of fluid dynamics. Fluid dynamics encompasses a diverse range of practical applications, including the computation of forces and moments, estimation of oil mass flow rates in pipelines, prediction of weather patterns, exploration of interstellar nebulae, and flow modeling. Neményi [22] provides a historical perspective, tracing the evolution of fundamental concepts and ideas in fluid dynamics, emphasizing the development of theoretical understanding over time. Building upon this theoretical foundation, Birkhoff [6] surveys the significant advancements and future potential of numerical fluid dynamics, underscoring the increasing reliance on computational methods to solve complex flow problems that defy analytical solutions. A practical application of these numerical techniques is demonstrated by Hofer et al. [13], who utilized the computational fluid dynamics and finite element analysis to study wall mechanics and fluid dynamics in end-to-side vascular anastomoses, establishing correlations between complex flow patterns and the development of intimal hyperplasia, a critical issue in biomedical engineering. Further showcasing the versatility of computational approaches, Liu et al. [18] employed computational fluid dynamics to investigate the unsteady aerodynamics of biological flight, specifically analyzing the flow around a hawkmoth's flapping wing during hovering to understand the vortex dynamics and force generation mechanisms in nature.

Building upon the foundational principles of fluid mechanics discussed earlier, a particular class of non-Newtonian fluids known as Casson fluids has garnered attention due to their unique rheological behavior. A fluid that exhibits

---

Received: 06 March 2025 ; Accepted: 10 August 2025.

* Corresponding author. Email: hassan.shahzad@cust.edu.pk, h.shahzad1996@gmail.com .

Table 1. **Nemoclature.**

a	positive constant	Γ_c	relaxation time for mass flux
B_0	magnetic field strength	Γ_e	relaxation time for heat flux
Cf_x	skin friction coefficient in x-direction	α_f	thermal diffusivity of fluid
C_w	concentration of nanoparticles at wall	ρ	density
Sh_x	local Sherwood number	$(c_p)_p$	specific heat coefficient of nanoparticle
Nu_x	local Nusselt number	λ_E	relaxation time parameter of temperature
C	concentration of nanoparticles	μ	dynamic viscosity
$(c_p)_f$	specific heat coefficient of fluid	ϵ	heat generation/absorption coefficient
D_B	Brownian diffusion coefficient	Γ	Inclined angle of magnetic field
f, g	velocity components in dimensionless form	γ_1	rotation parameter
q_r	radiative heat flux	σ	electrical conductivity of fluid
D_T	thermophoretic diffusion coefficient	ϕ	dimensionless concentration
Cf_y	skin friction coefficient in y-direction	η	similarity variable
k	thermal conductivity	θ	dimensionless temperature
k^*	mean absorption coefficient	μ_B	plastic dynamic viscosity
K_c^*	constant rate of chemical reaction	ν_f	kinematic viscosity of the nanofluid
u, v, w	velocity components	σ^*	Stefan-Boltzmann constant
C_∞	ambient concentration away from wall	β	Casson parameter
K_c	chemical reaction parameter	ρ_p	nanoparticle's density
T_∞	ambient fluid temperature	$(\rho c_p)_f$	fluid's heat capacity
q_w	wall heat flux	$(\rho c_p)_p$	nanoparticle's heat capacity
T	fluid temperature	τ	shear stress
T_w	surface temperature		

shear-thinning behavior, with theoretical infinite viscosity at zero shear rate and zero viscosity at infinite shear rate is referred to as a Casson fluid. In comparison to Newtonian-based nanofluid flow, Casson nanofluids offer greater advantages as cooling and friction-reducing agents. Casson fluids include various examples such as honey, jelly, sauce, and soup. Applications of Casson fluids span various sectors, including heat transfer and cooling systems, biomedical and pharmaceutical fields, the food industry, cosmetics and personal care, oil and gas processing, and automotive systems. The earliest work on Casson fluids was conducted by Casson et al. [8], who aimed to forecast the behavior of fluids resembling printing ink. A series-based solution to tackle heat and mass transfer phenomena in a non-Newtonian fluid was examined by Nadeem et al. [21] using the homotopy analysis method. According to their findings, variations in the Casson parameter, whether positive or negative, give rise to shifts in the stagnation point from its initial position. The study by Butt et al. [7] focused on elucidating the heat transfer properties in the context of boundary layer flow of a rotating Casson fluid over an extending surface using the shooting method combined with the fifth-order Runge–Kutta–Fehlberg method. Further, the analysis of non-Newtonian Casson fluid under the influence of MHD and a porous medium within a non-Fourier heat flux model was investigated by Vishalakshi et al. [32], who concluded that transverse and tangential velocities decrease under the influence of the Lorentz force.

Rotating fluid flows are of considerable interest due to their role in simulating engineering systems and natural processes influenced by rotational effects. The examination of fluid motion with rotation that gives rise to the Coriolis force finds noteworthy applications in a range of disciplines, including astrophysics, oceanography, and various geophysical situations. Moreover, this specific flow pattern over a stretching surface is employed across various domains. Wang [33] considered a two-dimensional stretchable surface to investigate the issue of rotating fluid flow. Moreover, when the rotational parameter outran unity, he gained a precise solution through analytical means, afterward contrasting it with the numerical technique. Zaimi et al. [34] employed the Keller-box method to analyze the rotating flow due to a stretching surface by considering a non-Newtonian viscoelastic fluid. Rashidi et al. [24] employed the law of increased Entropy to present an analysis of Entropy generation in the context of rotating nanofluid flow. Mabood et al. [19] conducted an investigation into the impact of Brownian motion and thermophoresis on the flow of rotating nanofluid. This analysis was carried out considering the presence of magnetic fields, radiation, viscous dissipation effects, heat source etc. The research executed by Das et al. [11] centered on investigating how transient hydromagnetic Couette flow of a viscous fluid is influenced by both magnetic field and rotation. The study revealed a substantial alteration in fluid velocity resulting from the combined effects. Ali et al. [2] investigated various types of nanoparticles to analyze how magnetic field within a rotational setup modifies Couette flow. The influence of thermophoresis and Brownian motion on mixed convective flow in magnetohydrodynamics over an inclined stretching surface, taking into account radiation and chemical reaction is analyzed by Sharma et al. [29]. The magnetohydrodynamics rotating flow over a stretching surface with a focus on fluctuating viscosity and nanoparticle aggregation is studied by Alqahtani et al. [3]. Heat conduction plays a critical role in many engineering and scientific applications, with Fourier's law traditionally serving as the foundational model that defines heat transfer through a linear relationship between heat flux and the temperature gradient [12]. However, a significant limitation of Fourier's law lies in its prediction of an infinite speed of thermal signal propagation, which contradicts the principle of causality, namely, that an effect cannot precede its cause. This theoretical drawback leads to non-physical results, such as instantaneous temperature changes across a medium. To overcome this issue, Cattaneo [9] introduced a modification that incorporates a finite thermal relaxation time, enabling heat signals to propagate at a finite speed. Subsequently, Christov [10] refined the model by employing objective time derivatives, yielding the Cattaneo–Christov heat flux model. This refined model aligns heat conduction theory with physical causality, allowing for realistic, time-dependent heat propagation. Utilizing this framework, Salmi et al. [25] employed the finite element method and observed that solute relaxation time exhibited a decreasing effect on the concentration field, which could be regulated by adjusting the solute relaxation parameter. Further exploration by Sohail et al. [31] demonstrated that an increase in the suction parameter leads to a decrease in both temperature and velocity profiles of a water-based ternary hybrid nanofluid under a three-dimensional non-Fourier heat conduction model. Akinbo and Olajuwon [1] examined the behavior of Walters' B fluid over an exponentially stretching sheet in a porous medium and reported that the temperature decreases with the inclusion of thermal relaxation time, as analyzed using the homotopy analysis method.

Radiation heat transfer is a crucial factor in many engineering applications, especially those involving high temperatures, where it significantly influences the overall heat transfer process. Its effects cannot be neglected when analyzing thermal systems such as combustion chambers, furnaces, and high-temperature manufacturing processes. Extensive research has been conducted to understand the impact of radiative heat transfer on fluid flow and thermal behavior. Hayat et al. [14] introduced a novel boundary condition, termed zero nanoparticle mass flux, to investigate its effect on three-dimensional flow of a viscoelastic fluid under nonlinear thermal radiation. Their results showed that the thermal boundary layer thickness increases with enhanced radiative heat intensity. Prasannakumara et al. [23] used the shooting method to study stagnation-point flow of a dusty fluid over a stretching sheet subjected to radiative heating and found that fluid temperature increases with an advancement of the melting process on the surface. Makinde and Eegunjobi [20], utilizing the Runge–Kutta–Fehlberg method, demonstrated that wall thermal slip conditions lead to a slight temperature reduction at the surface due to heat loss. Sheikholeslami and Shehzad [30] studied the effect of radiative heat transfer on ferrofluids via the Gauss–Seidel method and observed an increase in the Nusselt number with intensified thermal radiation. Islam et al. [15] investigated convective flow and thermal transport of nanofluids in a wavy triangular cavity, considering heat generation or absorption, reporting a 20.43% increase in heat transfer rate due to Brownian motion with 1% nanoparticle volume under radiative effects. Kumar et al. [17] optimized the heat transfer performance of aqueous nanofluids over a rotating disk by combining magnetic and radiation effects using numerical simulations and response surface optimization via the `bvp5c` function.

From the research mentioned earlier, many scientists have looked into how heat and mass transfer phenomena are exhibited in the case of Casson nanofluid flow on a stretching sheet. After thoroughly reviewing the existing literature, it is observed that no previous study incorporates the three-dimensional Cattaneo-Christov double diffusion flow within the Casson fluid model, particularly considering the porous medium. This research aims to cover this

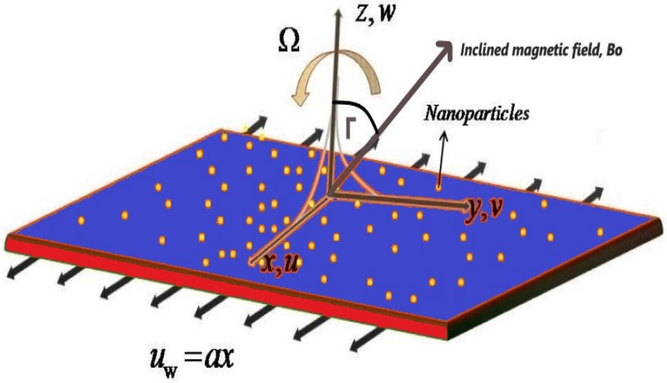

Figure 1. Geometry of physical model.

gap and comprehensively analyze the effects of viscous dissipation, thermal radiation, inclined magnetic field, heat source/sink, and chemical reaction within a non-Fourier framework.

2. Mathematical Modeling

Consider a three-dimensional time independent, incompressible laminar flow of an Casson nanofluid along a stretching smooth surface (See Fig. 1). In this study, the fluid has been considered to rotate around the z-axis with an angular velocity Ω within a flow region where z is restricted to values $z \geq 0$. Assume that the velocity of extending sheet is represented by $U_w(x) = ax$. An inclined magnetic field of magnitude B_0 is applied in z- axis direction. Since the classical Fourier law assumes infinite thermal propagation speed, the Cattaneo-Christov double diffusion model is utilized to incorporate finite thermal and solutal relaxation times, λ_E and λ_C, respectively. This provides a more physically realistic description of heat and mass transfer. The energy transport equation includes effects of thermal radiation, heat generation, and the Cattaneo-Christov double diffusion model. Similarly, the mass transport accounts for delayed solutal diffusion through the relaxation parameter Γ_c. The governing equations under the assumptions stated above for mass, momentum, energy and concentration are as follows [4, 16, 26, 28]:

$$u_x + v_y + w_z = 0, \tag{2.1}$$

$$uu_x + vu_y + wu_z - 2\Omega v = \nu\left(1 + \frac{1}{\beta}\right)u_{zz} - \frac{\mu}{\rho_f}\frac{u}{k} - \frac{\sigma B_0^2}{\rho_f} usin^2(\Gamma), \tag{2.2}$$

$$uv_x + vv_y + wv_z + 2\Omega u = \nu\left(1 + \frac{1}{\beta}\right)v_{zz} - \frac{\mu}{\rho_f}\frac{v}{k} - \frac{\sigma B_0^2}{\rho_f} vsin^2(\Gamma), \tag{2.3}$$

$$\begin{aligned} &uT_x + vT_y + wT_z + \Gamma_e\Big[u^2T_{xx}v^2T_{yy}w^2T_{zz} + 2uvT_{xy} + 2uwT_{xz} + 2vwT_{yz} \\ &+ \left(uw_x + vw_y + ww_z\right)T_z + \left(uv_x + vv_y + wv_z\right)T_y + \left(uu_x + vu_y + wu_z\right)T_x\Big] \\ &= \left[\left(\alpha + \frac{16\sigma^* T^3}{3K^*\left(\rho c_p\right)_f}\right)T_z\right]_z + \tau\left[D_B T_z C_z + \frac{D_T}{T_\infty}\left(T_z\right)^2\right] + \frac{Q}{(\rho c_p)_f}(T - T_\infty) \\ &+ \frac{\mu}{\left(\rho c_p\right)_f}\left(1 + \frac{1}{\beta}\right)\left(\left(u_z\right)^2 + \left(v_z\right)^2\right) + \frac{\sigma B_0^2}{\left(\rho c_p\right)_f}\left(u^2 + v^2\right) sin^2(\Gamma), \end{aligned} \tag{2.4}$$

$$uC_x + vC_y wC_z + \Gamma_c\Big[u^2C_{xx} + v^2C_{yy} + w^2C_{zz} + 2uvC_{xy} + 2vwC_{yz} + 2uwC_{xz}$$

$$+\left(uu_x+vu_y+wu_z\right)C_x+\left(uv_x+vv_y+wv_z\right)C_y+\left(uw_x+vw_y+ww_z\right)C_z\Big]$$
$$=D_BC_{zz}+\frac{D_T}{T_\infty}T_{zz}-K_c^*\left(C-C_\infty\right). \tag{2.5}$$

In the above equation, v and u denote the velocity components along the y and x directions, respectively, ν represents the kinematic viscosity, $K=\frac{\nu_f}{ak}$ is the porous medium parameter and Q is the heat generation/absorption coefficient, $\beta=\mu_B\sqrt{2\pi_c}/\frac{\partial p}{\partial y}$ is the Casson fluid parameter.
The associated boundary conditions are:

$$\begin{cases} v=0,\ u=U_w(x),\ w=0,\ C=C_w,\ T=T_w,\ at\ z=0, \\ u\to 0,\ v\to 0,\ C\to C_\infty,\ T\to T_\infty as\ z\to\infty. \end{cases} \tag{2.6}$$

The boundary conditions in Equation (2.6) define the physical constraints at the plate surface and in the far-field region. At the surface, the no-slip condition is imposed with a specified stretching velocity $u=U_w(x)$, while the normal velocity v and cross-flow component w are both zero. Additionally, the fluid temperature and concentration are maintained at the surface values T_w and C_w, respectively. Far from the surface, the velocity components diminish to zero, while the temperature and concentration gradually approach their ambient levels T_∞ and C_∞, respectively, ensuring a physically realistic flow and thermal field.

Following similarity transformations have been considered [5]:

$$\begin{cases} \eta=\sqrt{\frac{a}{\nu}}z,\ \phi(\eta)=\dfrac{C-C_\infty}{C_w-C_\infty},\ T=T_\infty\left(1+\left(\theta_w-1\right)\theta(\eta)\right), \\ w=-\sqrt{a\nu}\left(\eta\right),\ v=axg(\eta),\ u=axf'(\eta), \end{cases} \tag{2.7}$$

where θ_w=$\frac{T_w}{T_\infty}>1$ denotes the temperature ratio parameter.

The radiative heat flux is

$$q_r=-\frac{4\sigma^*}{3k^*}\left(\frac{\partial T^4}{\partial z}\right). \tag{2.8}$$

By employing Taylor series expansion and neglecting higher-order terms, T^4 is approximated as $T^4=4T_\infty^3T-3T_\infty^4$. Simplifying Eq. (2.8) under this approximation gives:

$$\frac{\partial q_r}{\partial z}=-\frac{16\sigma^*T^3}{3k*}T_{zz}. \tag{2.9}$$

By using the transformation (2.7), the resulting non-dimensional form of the governing equations is given below:

$$\left(1+\frac{1}{\beta}\right)\frac{\partial^3 f}{\partial\eta^3}-\left(\frac{\partial f}{\partial\eta}\right)^2+f\frac{\partial^2 f}{\partial\eta^2}+2\gamma_1 g-K\frac{\partial f}{\partial\eta}-M\frac{\partial f}{\partial\eta}sin^2(\Gamma)=0, \tag{2.10}$$

$$\left(1+\frac{1}{\beta}\right)\frac{\partial^2 g}{\partial\eta^2}+f\frac{\partial g}{\partial\eta}-\frac{\partial f}{\partial\eta}g-2\gamma_1\frac{\partial f}{\partial\eta}-Kg-Mgsin^2(\Gamma)=0, \tag{2.11}$$

$$\frac{\partial}{\partial\eta}\left(1+Rd\left(1-(1-\theta_w)\theta\right)^3\right)\frac{\partial\theta}{\partial\eta}+Pr\Bigg[f\frac{\partial\theta}{\partial\eta}+N_b\frac{\partial\theta}{\partial\eta}\frac{\partial\phi}{\partial\eta}+N_t\left(\frac{\partial\theta}{\partial\eta}\right)^2+Ec\Bigg(\left(1+\frac{1}{\beta}\right)\left(\left(\frac{\partial^2 f}{\partial\eta^2}\right)+\left(\frac{\partial g}{\partial\eta}\right)^2\right)$$
$$+M\left(\left(\frac{\partial f}{\partial\eta}\right)^2+g^2\right)\Bigg)-\lambda_E\left[f^2\frac{\partial^2\theta}{\partial\eta^2}+f\frac{\partial f}{\partial\eta}\frac{\partial\theta}{\partial\eta}\right]+\epsilon\theta\Bigg]=0, \tag{2.12}$$

$$\frac{\partial^2\phi}{\partial\eta^2}+Sc\left[f\frac{\partial\phi}{\partial\eta}-\lambda_C\left(f^2\frac{\partial^2\phi}{\partial\eta^2}+f\frac{\partial f}{\partial\eta}\frac{\partial\phi}{\partial\eta}\right)-K_c\phi\right]+\frac{N_t}{N_b}\frac{\partial^2\theta}{\partial\eta^2}=0. \tag{2.13}$$

Similarly, the boundary conditions after treatment by (2.7), get the following form:

$$\begin{cases} f(0)=0,\ g(0)=0,\ \dfrac{\partial f}{\partial \eta}=1,\ \phi(0)=0,\ \theta(0)=0,\ as\ \eta\to 0. \\ \dfrac{\partial f}{\partial \eta}\to 0,\ g\to 0,\ \theta\to 0,\ \phi\to 0,\ as\ \eta\to\infty, \end{cases} \tag{2.14}$$

where Sc is the Schmidt number, Rd is the radiation parameter, Nb is the Brownian motion parameter, Pr is the Prandtl number, Nt is the thermophoresis parameter, Ec is the Eckert number and M is the magnetic parameter. The dimensionless parameters arising in (2.10)-(2.13) are given as:

$$\begin{cases} \gamma_1=\dfrac{\Omega}{a},\ M=\dfrac{\sigma B_0^2}{\rho a},\ K=\dfrac{\nu}{ak},\ Rd=\dfrac{16T_\infty^3\sigma^*}{3kk^*},\ Nt=\dfrac{\tau D_T\left(T_w-T_\infty\right)}{\nu T_\infty}, \\ Nb=\dfrac{\tau D_B\left(C_w-C_\infty\right)}{\nu},\ Ec=\dfrac{U_w^2}{\left(c_p\right)_f\left(T_w-T_\infty\right)},\ K_c=\dfrac{K_c^*}{a}, \\ \lambda_C=a\Gamma_c,\ \lambda_E=a\Gamma_e,\ Sc=\dfrac{\nu}{D_B},\ Pr=\dfrac{\nu}{\alpha},\ \epsilon=\dfrac{Q}{a(\rho c_p)_f}. \end{cases} \tag{2.15}$$

Here, the skin friction coefficient C_f on the surface expressed in both the x and y directions is defined respectively as:

$$C_{fx}=\frac{\tau_{wx}}{\rho U_w^2},\quad C_{fy}=\frac{2\tau_{wy}}{\rho U_w^2}. \tag{2.16}$$

The wall shear stresses τ_{wx} and τ_{wy} in their respective directions are defined as

$$\tau_{wx}=\mu_B\left(1+\frac{1}{\beta}\right)\left(\frac{\partial u}{\partial z}\right)_{z=0},\ \tau_{wy}=\mu_B\left(1+\frac{1}{\beta}\right)\left(\frac{\partial v}{\partial z}\right)_{z=0}. \tag{2.17}$$

The skin friction coefficients in dimensionless form, are given by

$$\left(Re_x\right)^{\frac{1}{2}}C_{fx}=\left(1+\frac{1}{\beta}\right)\left.\frac{\partial^2 f}{\partial \eta^2}\right|_{\eta=0},\ \left(Re_x\right)^{\frac{1}{2}}C_{fy}=\left(1+\frac{1}{\beta}\right)\left.\frac{\partial g}{\partial \eta}\right|_{\eta=0}. \tag{2.18}$$

where, $Re_x=\frac{U_w^2}{a\nu}$ depends on the stretching velocity U_w.
The remaining physical quantities of interest are as follows:

$$Nu_x=\frac{U_w q_w}{ak(T_w-T_\infty)},\ Sh_x=\frac{q_m x}{D_B\left(C_w-C_\infty\right)}. \tag{2.19}$$

The wall thermal heat and mass fluxes, denoted by $q_w,\ q_m$ and q_n respectively, are defined as:

$$q_w=-k_f\left(\frac{\partial T}{\partial z}\right)_{z=0}+\left(q_r\right)_w,\qquad q_m=-D_B\left(\frac{\partial C}{\partial z}\right)_{z=0}. \tag{2.20}$$

As a result, the non-dimensional forms of the formulae in (2.19) are as follows:

$$Nu_xRe_x^{-1/2}=-\left(1+Rd\theta_w^2\right)\theta'(0),\ Sh_xRe_x^{-1/2}=-\phi'(0). \tag{2.21}$$

3. Solution Methodology

The numerical computation of Equations (2.10)–(2.13), governed by the boundary conditions (2.14), is carried out using the shooting method, which integrates the fourth-order Runge–Kutta technique with Newton's method. This method is chosen for its relatively low computational cost and high accuracy in solving boundary value problems transformed into initial value problems. To facilitate numerical calculations, Equations (2.10) and (2.11) are reduced to first-order equations by u:sing the following substitution:

$$f=Z_1, f'=Z_1'=Z_2, f''=Z_2'=Z_3, g=Z_4, g'=Z_4'=Z_5.$$

As a consequence of the above notations, the following system of ODEs is acquired for Eqs. (2.10) and (2.11):

$$\begin{cases} Z_1' = Z_2,\ Z_1(0) = 0, \\ Z_2' = Z_3,\ Z_2(0) = 1, \\ Z_3' = \dfrac{\beta}{1+\beta}\Big(Z_2^2 - Z_1Z_3 - 2\gamma_1 Z_4 + \kappa Z_2 + MZ_2 sin^2(\Gamma)\Big),\ Z_3(0) = r, \\ Z_4' = Z_5,\ Z_4(0) = 0, \\ Z_5' = \dfrac{\beta}{1+\beta}\Big(-Z_1Z_5 + Z_2Z_4 + 2\gamma_1 Z_2 + \kappa Z_4 + MZ_4 sin^2(\Gamma)\Big),\ Z_5(0) = m, \end{cases} \tag{3.1}$$

where r and m are the missing initial conditions. The above initial value problem will be numerically solved by the RK-4 method. The domain of current problem is considered to be bounded i.e. $[0, \eta_\infty]$, where η_∞ is a positive number for which the variation in the solution is negligible after $\eta = \eta_\infty = 6$. The missing conditions r and m are assumed to satisfy the following relation:

$$Z_2(\eta_\infty, r, m) = 0,\ Z_4(\eta_\infty, r, m) = 0.$$

The Newton's iterative formula for the updation of r and m, takes the following form:

$$\begin{bmatrix} r \\ m \end{bmatrix}_{(n+1)} = \begin{bmatrix} r \\ m \end{bmatrix}_{(n)} - \begin{bmatrix} \frac{\partial Z_2}{\partial r} & \frac{\partial Z_2}{\partial m} \\ \frac{\partial Z_4}{\partial r} & \frac{\partial Z_4}{\partial m} \end{bmatrix}^{-1}_{(n)} \begin{bmatrix} Z_2 \\ Z_4 \end{bmatrix}_{(n)},$$

In order to incorporate Newton's method the following derivatives have been introduced:

$$\frac{\partial Z_1}{\partial r} = Z_6,\ \frac{\partial Z_2}{\partial r} = Z_7,\ \frac{\partial Z_3}{\partial r} = Z_8,\ \frac{\partial Z_4}{\partial r} = Z_9,\ \frac{\partial Z_5}{\partial r} = Z_{10},$$
$$\frac{\partial Z_1}{\partial m} = Z_{11},\ \frac{\partial Z_2}{\partial m} = Z_{12},\ \frac{\partial Z_3}{\partial m} = Z_{13},\ \frac{\partial Z_4}{\partial m} = Z_{14},\ \frac{\partial Z_5}{\partial m} = Z_{15}.$$

Hence the Newton's iterative formula takes the following form by using the above notations:

$$\begin{bmatrix} r \\ m \end{bmatrix}_{(n+1)} = \begin{bmatrix} r \\ m \end{bmatrix}_{(n)} - \begin{bmatrix} Z_7 & Z_{12} \\ Z_9 & Z_{14} \end{bmatrix}^{-1}_{(n)} \begin{bmatrix} Z_2 \\ Z_4 \end{bmatrix}_{(n)}. \tag{3.2}$$

Differentiating (3.1) first w.r.t. r and then w.r.t. m, the following system of ten first order ODEs is obtained, which when sloved by the RK-4 method helps to update r and m by using (3.2):

$$Z_6' = Z_7,\ Z_6(0) = 0.$$
$$Z_7' = Z_8,\ Z_7(0) = 0.$$
$$Z_8' = \frac{\beta}{1+\beta}\Big(2Z_2Z_7 - Z_6Z_3 - Z_1Z_8 - 2\gamma_1 Z_9 + \kappa Z_7 + MZ_7 sin^2(\Gamma)\Big),\ Z_8(0) = 1.$$
$$Z_9' = Z_{10},\ Z_9(0) = 0.$$
$$Z_{10}' = \frac{\beta}{1+\beta}\Big(Z_2Z_9 - Z_1Z_{10} + Z_7Z_4 - Z_6Z_5 + 2\gamma_1 Z_7 + \kappa Z_9 + MZ_9 sin^2(\Gamma)\Big),\ Z_{10}(0) = 0.$$
$$Z_{11}' = Z_{12},\ Z_{11}(0) = 0.$$
$$Z_{12}' = Z_{13},\ Z_{12}(0) = 0.$$
$$Z_{13}' = \frac{\beta}{1+\beta}\Big(2Z_2Z_{12} - Z_{11}Z_3 - Z_1Z_{13} - 2\gamma_1 Z_{14} + \kappa Z_{12} + MZ_{12} sin^2(\Gamma)\Big),\ Z_{13}(0) = 0.$$
$$Z_{14}' = Z_{15},\ Z_{14}(0) = 0.$$
$$Z_{15}' = \frac{\beta\Big(Z_2Z_{14} - Z_1Z_{15} + Z_{12}Z_4 + -Z_{11}Z_5 + 2\gamma_1 Z_{12} + \kappa Z_{14} + MZ_{14} sin^2(\Gamma)\Big)}{1+\beta}\ Z_{15}(0) = 1.$$

TABLE 2. Computational results for grid independence test.

Interval size	Skin friction along x	Skin friction along y	Nusselt number	Sherwood number
0.12	-2.48263982	-0.66128645	0.10704113	2.10943312
0.03	-2.48263965	-0.66128680	0.07143689	1.98247806
0.01	-2.48263965	-0.66128680	0.06341752	1.95631411
0.008	-2.48263965	-0.66128680	0.062412380	1.95309335
0.006	-2.48263965	-0.66128680	0.06180899	1.95116614

TABLE 3. Comparison of current outcomes of $-f''(0)$ with those of Shahzad and Sagheer [27] when $\gamma_1 = k = \beta = 0$ and $\Gamma = \pi/2$.

M	Shahzad and Sagheer. [27]	Present outcomes
0.0	1.00048	1.00048
0.2	1.09559	1.09560
0.5	1.22477	1.22478
1.0	1.41423	1.41422
1.2	1.48325	1.48324
1.5	1.58114	1.58114

TABLE 4. Comparison of current outcomes of $f''(0)$ with Archana et al. [5] when $M = \beta = k = 0$ and $\Gamma = \pi/2$.

γ_1	Archana et al. [5]		Present outcomes	
	$f''(0)$	$g'(0)$	$f''(0)$	$g'(0)$
0	-1.00048	0	-1.00048	0
0.5	-1.13848	-0.51268	-1.13848	-0.51268

The iterative process is repeated until the criteria listed below is met:

$$max\{| Z_2(\eta_\infty, r^n, m^n) |, | Z_4(\eta_\infty, r^n, m^n) |\} < \epsilon,$$

for an arbitrarily small positive value of ϵ. Here, ϵ is taken as 10^{-10}.
Equations (2.12) and (2.13) are solved simultaneously, by using the same procedure.
To ensure the reliability of the numerical methodology employed in this study, a grid independence test is conducted, as presented in Table 2. Furthermore, the accuracy of the current results is validated through comparison with previously published data in Refs. [5, 27], shown in Tables 3 and 4. In addition, Figure 2 illustrates the residual error, confirming the stability and convergence of the numerical scheme.

4. RESULTS AND DISCUSSION

In this section, we thoroughly discuss the influence of some crucial dimensionless parameters on the skin friction coefficients $Re_x^{\frac{1}{2}} C_{f_x}$, $Re_y^{\frac{1}{2}} C_{f_y}$, Nusselt number $Re_x^{-\frac{1}{2}} Nu_x$ and Sherwood number $Re_x^{-\frac{1}{2}} Sh_x$ through different graphs and tables.

4.1. Analysis of computational and graphical results of physical quantities.

Table 5 presents the influence of the Casson parameter β, rotation parameter γ_1, magnetic parameter M, porous medium parameter K, and inclination angle Γ on the skin friction coefficients $Re_x^{\frac{1}{2}} C_{f_x}$ and $Re_y^{\frac{1}{2}} C_{f_y}$, along with the intervals I_f and I_g , from which the missing initial slopes r and m can be selected. An increase in the Casson parameter β, which is associated with higher yield stress, enhances the fluid resistance, resulting in a rise of approximately 5.71% to 13.37% in both skin friction coefficients when β is increased by 25% to 60%, as also depicted in Figure 3. On the other hand, an increase in the

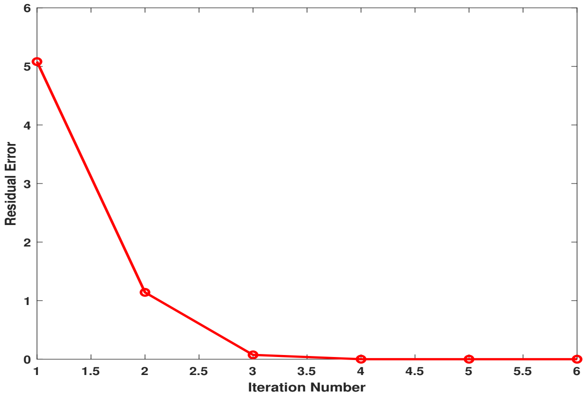

FIGURE 2. Residual error against iteration number when $M = \beta = k = 0.5$

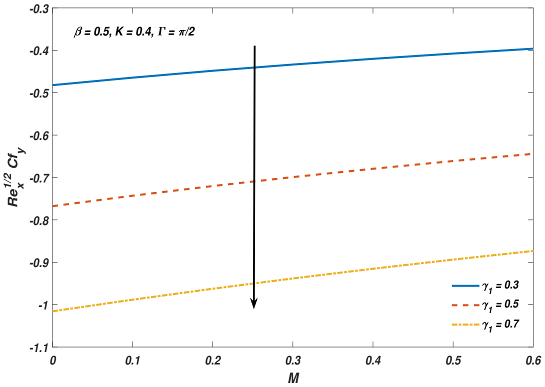

FIGURE 3. Cf_y distribution against γ_1 and M.

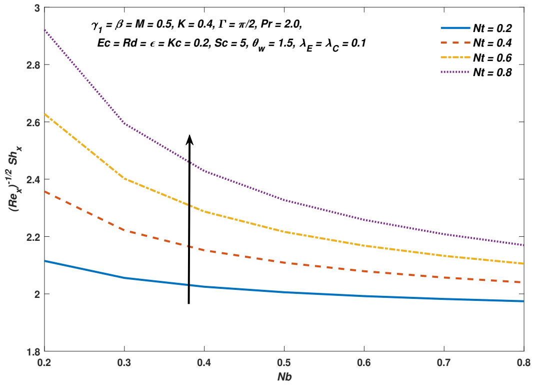

FIGURE 4. Sh_x distribution against Nb and Nt.

rotation parameter γ_1 leads to a reduction in skin friction along the surface, with a maximum decline of around 4.96% due to the Coriolis force resisting the flow motion.

Table 6 elaborates the behavior of the Nusselt and Sherwood numbers under the variation of different dimensionless parameters. A rise in the temperature difference parameter leads to a significant enhancement in the rate of heat transfer, with the Nusselt number increasing by approximately 37.55% to 64.50%, despite the parameter itself varying only 5.59% to 6.67%. In contrast, the Brownian motion parameter Nb causes a decline in the heat transfer rate due to enhanced random particle motion. However, the thermophoresis parameter Nt contributes to a notable rise in the heat transfer rate, as thermal gradients drive nanoparticles away from the hot region, boosting thermal energy distribution, as also depicted in Figure 4. The rate of mass transfer, represented by the Sherwood number, is observed to increase slightly by about 0.26% to 0.39% with higher values of the concentration relaxation time parameter λ_C, indicating slower diffusion due to delayed mass response. Furthermore, an increase in the chemical reaction parameter K_c results in a higher rate of mass transfer, as stronger reactions enhance species consumption at the surface, as shown in Table 6.

4.2. **Velocity distribution.** Figure 5 shows a decreasing behaviour of the velocity distribution f' while increasing the values of β. Physically, the Casson parameter β is influenced by the yield stress, which creates an opposing force that

TABLE 5. Results of $Re_x^{\frac{1}{2}} C_{fx}$ and $Re_x^{\frac{1}{2}} C_{fy}$ for various parameters.

β	γ_1	M	K	Γ	$Re_x^{\frac{1}{2}} C_{fx}$	$Re_x^{\frac{1}{2}} C_{fy}$	I_f	I_g
0.5	0.5	0.5	0.4	$\pi/2$	-2.48263	-0.66128	[-1.70, 1.90]	[-2.30, 1.70]
0.8					-2.15059	-0.57329	[-1.90, 1.60]	[-2.50, 1.90]
1.0					-2.02772	-0.54057	[-1.80, 2.30]	[-2.70, 0.60]
	0.3				-2.42473	-0.40770	[-1.10, 2.60]	[-3.10, 2.20]
	0.6				-2.51875	-0.78023	[-2.20, 2.80]	[-2.60, 3.00]
	0.9				-2.64364	-1.10502	[-2.30, 3.10]	[-2.40, 1.70]
		0			-2.19783	-0.76779	[-1.20, 3.50]	[-2.80, 2.70]
		0.4			-2.42669	-0.67951	[-1.80, 3.30]	[-3.10, 3.30]
		0.8			-2.64515	-0.61357	[-1.80, 3.60]	[-2.00, 1.10]
			0.6		-2.59172	-0.62842	[-2.20, 3.80]	[-2.60, 3.10]
			0.8		-2.69784	-0.59963	[-2.30, 3.40]	[-1.90, 1.20]
			1.0		-2.80102	-0.57418	[-2.00, 3.30]	[-2.70, 3.30]
				$\pi/6$	-2.27046	-0.73718	[-2.50, 3.10]	[-3.10, 3.20]
				$\pi/4$	-2.34222	-0.70947	[-2.10, 2.70]	[-1.80, 1.50]
				$\pi/3$	-2.41297	-0.68427	[-2.20, 3.00]	[-3.20, 3.30]

results in a decrease in the velocity of the fluid with a gradual increase in β values. The effect of the same parameter on the coupled velocity distribution $g(\eta)$ is reflected in Figure 5, which reveals an upward trend with respect to β as mentioned in this figure.

The consequence of altering the magnetic parameter M for the velocity distributions f' and g can be visualized in Figure 6, showcasing a decrease in $f^{'}$ and an increase in g due to an inclination in M. This occurs because a drag force which is termed as the Lorentz force appears due to the applied magnetic field generated by the motion of charges. This force causes a decrement in the magnitude of the velocity along the x-direction. Figure 7 depicts the velocity distributions for varying values of the porous medium parameter K. The distribution denoted as f' exhibits a decreasing trend as K increases, while g demonstrates an increment with rising values of K. This occurs because the increasing permeability of the porous medium increases the flow rate of fluid through it, assuming a constant pressure gradient. The influence of the rotation parameter γ_1 on f' and g is portrayed in Figures 8. It has been observed that an increase in the rotation parameter leads to a deterioration in the velocity along the x-direction.

4.3. **Temperature distribution.** The Figure 9 indicates that increasing the Casson parameter brings about an enhancement in the thermal boundary layer thickness, leading to a higher fluid temperature. This occurs because a larger Casson parameter signifies increased fluid yield stress, which restricts momentum diffusion more than thermal diffusion, thereby allowing heat to spread more effectively. Figure 10 illustrates the behavior of the temperature distribution θ for variations in θ_w. As this parameter increases, the temperature also experiences an observable hike. Physically, θ_w reflects the wall-to-ambient temperature ratio, and a rise in this parameter promotes heat transfer from the wall into the fluid, thus raising the local fluid temperature. Figures 11 demonstrate the influence of Nb. As Nb increases, the temperature distribution rises. The occurrence of Brownian motion in the fluid is attributed to the presence of nanoparticles. Brownian motion enhances the random molecular agitation, which facilitates thermal energy dispersion, leading to a higher temperature within the fluid. Figure 12 expresses the relation between the relaxation time parameter λ_E and the temperature distribution θ, where θ shows a decreasing trend with rising λ_E. Physically, we can say that when λ_E attains higher values, the system possesses a non-conductive feature that results in contraction

TABLE 6. Results of $Re_x^{-\frac{1}{2}}Nu_x$ and $Re_x^{-\frac{1}{2}}Sh_x$ for various parameters.

β	γ_1	M	K	Γ	Rd	θ_w	Pr	Nb	Nt	Ec	Sc	λ_E	ϵ	λ_C	K_c	$Re_x^{-\frac{1}{2}}Nu_x$	$Re_x^{-\frac{1}{2}}Sh_x$
0.5	0.5	0.5	0.4	$\pi/2$	0.2	1.5	2.0	0.5	0.5	0.2	5.0	0.1	0.2	0.1	0.2	0.01724	1.96539
0.6																0.01285	1.95535
	0.2															0.06499	1.96819
	0.3															0.05309	1.96747
		0.0														0.14902	1.96936
		0.3														0.06959	1.96686
			0.3													0.02879	1.96765
			0.5													0.00547	1.96319
				$\pi/6$												0.11585	1.96828
				$\pi/4$												0.08277	1.96726
					0.4											0.06359	1.95224
					0.5											0.07338	1.94802
						1.6										0.02836	1.96224
						1.7										0.03901	1.95920
							1.0									0.05238	1.93649
							1.5									0.04469	1.95296
								0.2								0.08835	2.00692
								0.3								0.05054	1.97964
									0.0							0.05179	1.90933
									0.05							0.03431	1.93689
										0.0						0.40286	1.92442
										0.05						0.30721	1.93453
											3.0					0.00517	1.49949
											4.0					0.01153	1.74717
												0.2				0.03533	1.96580
												0.3				0.05267	1.96630
													0.0			0.26899	1.94262
													0.1			0.15202	1.95344
														0.13		0.01758	1.97309
														0.15		0.01782	1.97828
															0.1	0.01203	1.69165
															0.0	0.01479	1.83341

of the thermal distribution. This is due to the Cattaneo-Christov theory, where a larger λ_E introduces a thermal relaxation effect, limiting the instantaneous conduction of heat and hence suppressing the temperature field. Figure 13 displays the impact of the Prandtl number Pr on the temperature distribution θ. Both the thickness of the thermal boundary layer and the temperature distribution decrease as Pr increases. A higher Pr implies that momentum diffuses more rapidly than heat, which restricts thermal diffusion and reduces fluid temperature. Figure 14 reflects a

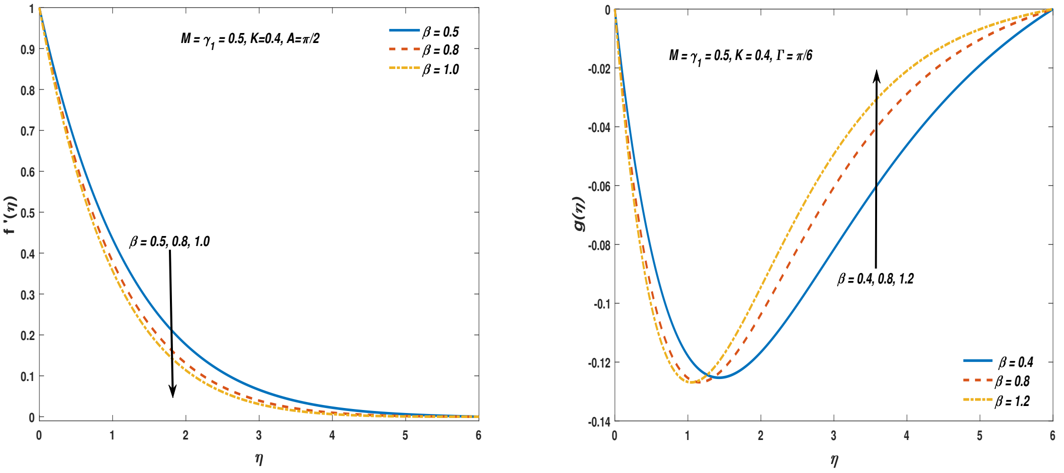

(a) (b)

Figure 5. Velocity distributions against β.

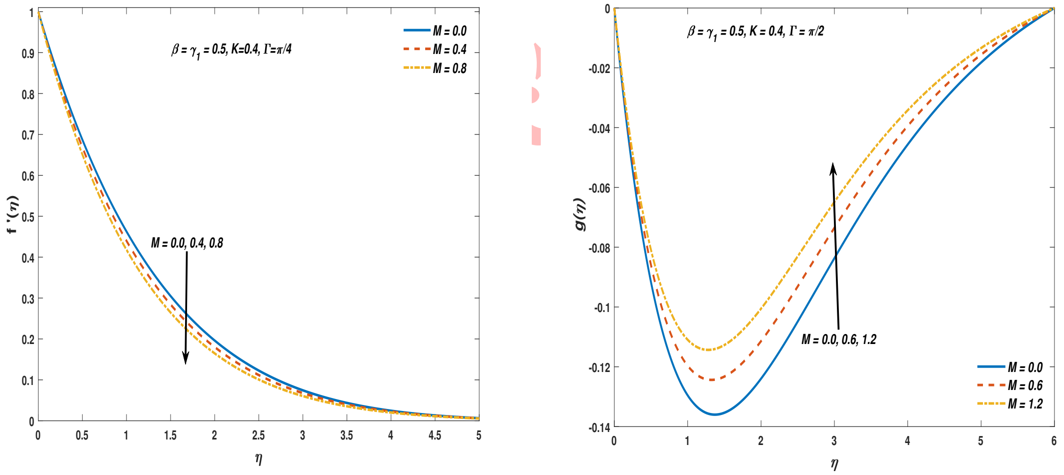

(a) (b)

Figure 6. Velocity distributions against M.

variation in the temperature distribution θ due to the radiation parameter Rd. As Rd increases, more heat energy is emitted into the flow, resulting in an uplifted temperature distribution. This increase in Rd amplifies radiative heat flux, enhancing energy transfer throughout the fluid medium. For increasing values of the heat generation/absorption parameter ϵ, Figure 15 depicts that the temperature distribution θ increases. Clearly, a positive change in the heat sink parameter results in increased heat generation within the liquid, contributing to the improvement of the thermal boundary layer thickness and temperature distribution. This internal heat source supplements thermal energy

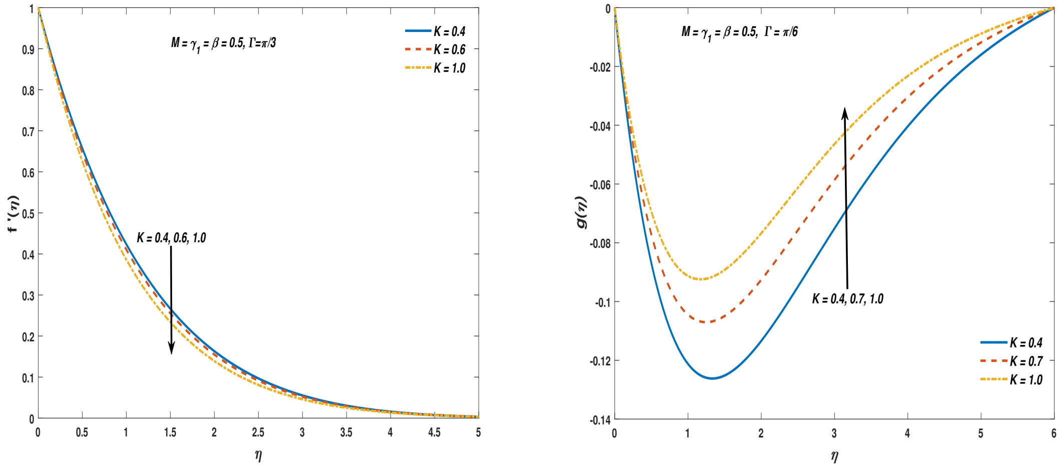

(a) (b)

FIGURE 7. Velocity distributions against K.

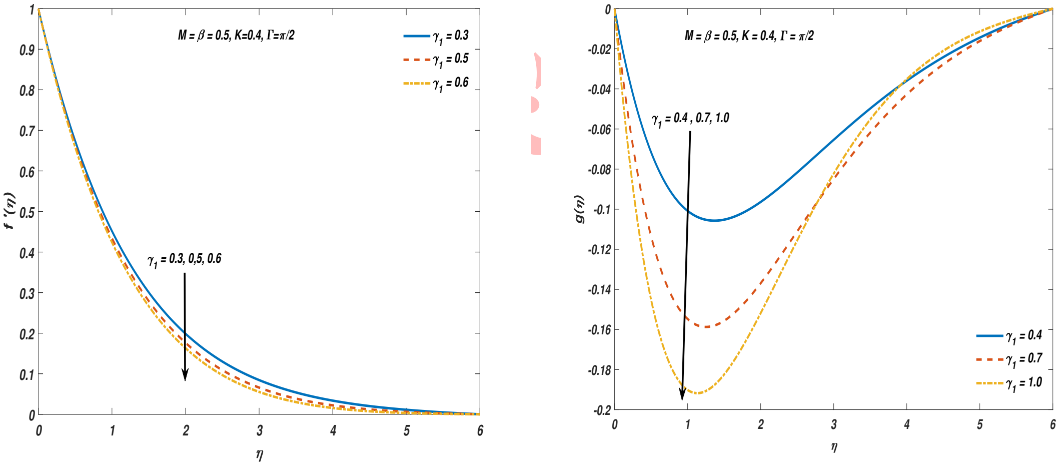

(a) (b)

FIGURE 8. Velocity distributions against γ_1.

within the fluid, thereby raising its overall temperature. The influence of the Eckert number Ec on the temperature distribution θ showcases a rising pattern in θ as mentioned in Figure 16. The temperature distribution escalates as the value of the Eckert number goes up. This is because a larger Ec reflects more viscous dissipation, where kinetic energy is converted into internal heat, directly enhancing the fluid's thermal state.

4.4. **Concentration distribution.** A decline in the concentration distribution ϕ is evident as the Schmidt parameter Sc increases, as illustrated in Figure 17. A higher Sc value corresponds to a fluid with relatively lower mass diffusivity,

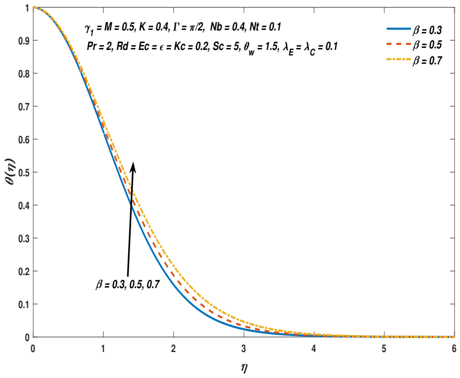

FIGURE 9. Temperature distribution against β

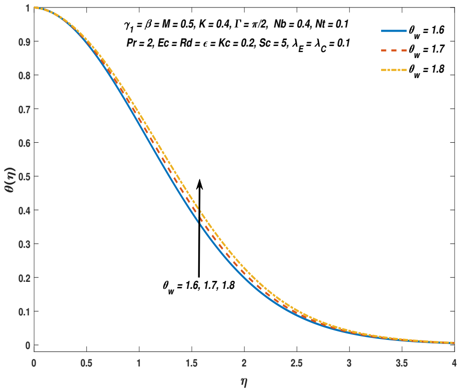

FIGURE 10. Temperature distribution against θ_w

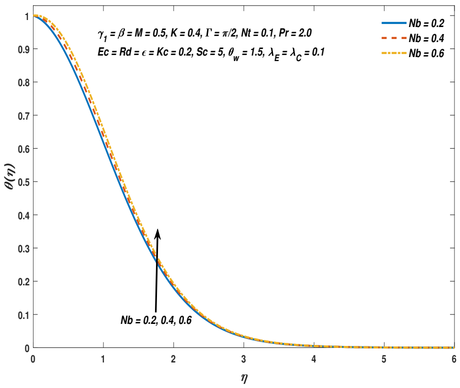

FIGURE 11. Temperature distribution against Nb

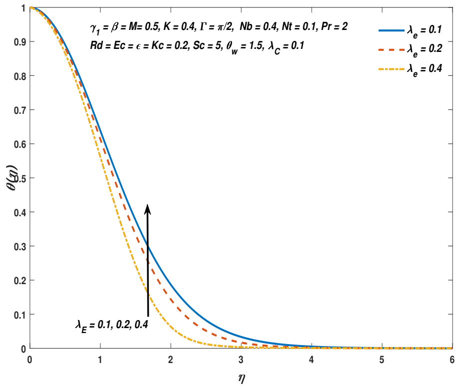

FIGURE 12. Temperature distribution against λ_E

which hinders the mobility of nanoparticles, thereby reducing the spread of concentration within the boundary layer. Figure 18 illustrates that an increase in the chemical reaction parameter K_c leads to a decreasing trend in ϕ. With higher K_c, the rate of chemical reaction accelerates, promoting the consumption of reactant species and diminishing the concentration level throughout the domain. Figure 19 presents the effect of the concentration relaxation time parameter λ_C on ϕ. It is evident that ϕ decreases as λ_C increases. Larger values of λ_C delay the diffusion process due to thermal inertia effects under the Cattaneo-Christov framework, thereby restricting mass transfer and leading to a thinner concentration profile. Figure 20 displays the influence of the thermophoresis parameter Nt on the concentration distribution. As Nt increases, ϕ undergoes an enhancement. This is attributed to stronger thermophoretic forces, which drive nanoparticles from the heated region towards the cooler region, causing an accumulation of particles that thickens the concentration boundary layer.

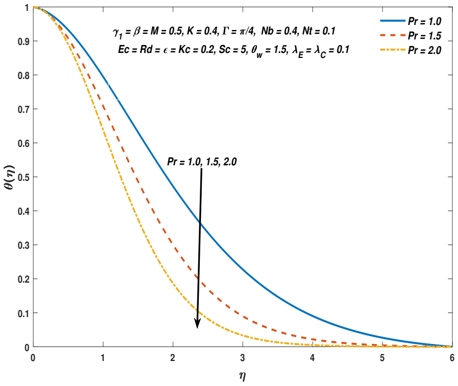

FIGURE 13. Temperature distribution against Pr

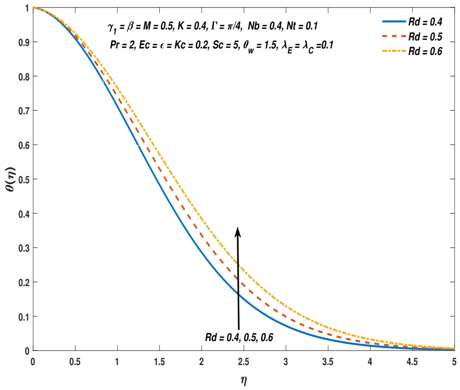

FIGURE 14. Temperature distribution against Rd

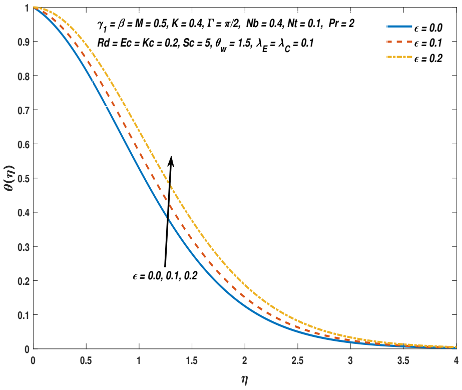

FIGURE 15. Temperature distribution against ϵ

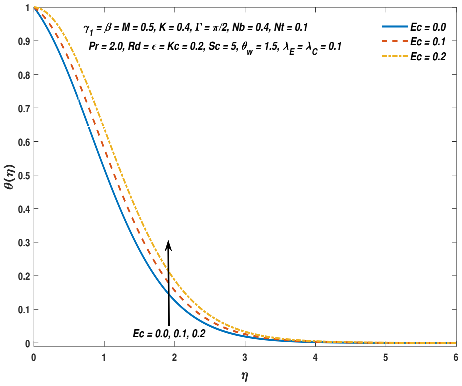

FIGURE 16. Temperature distribution against Ec

5. CONCLUSION

A detailed examination is conducted to investigate the rotational behavior of non-Newtonian Casson nanofluid in the presence of Cattaneo-Christov double diffusion, inclined magnetic filed, viscous dissipation, porous medium and rate of chemical reaction. The current study's notable results are listed below:

- An increase in the porous medium permeability K and rotation parameter both decrease $f'(\eta)$, while $g(\eta)$ increases with K, indicating higher transverse flow due to increased permeability and rotational influence.
- Increasing the Casson parameter β by 25% to 60% leads to a 5.71% to 13.37% rise in both skin friction coefficients, indicating enhanced fluid resistance due to higher yield stress.
- Larger thermal relaxation time parameter (λ_E) reduces the temperature distribution by introducing a delay in heat conduction, limiting instantaneous thermal diffusion.
- The Nusselt number improves by 37.55% to 64.50% with a modest increase (5.59% to 6.67%) in the temperature difference parameter, reflecting significantly enhanced heat transfer.
- Increasing the Schmidt number Sc reduces the concentration distribution ϕ due to lower mass diffusivity, limiting the nanoparticle mobility.

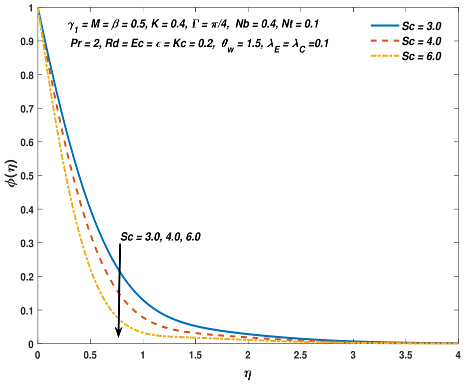

FIGURE 17. Concentration distribution against Sc

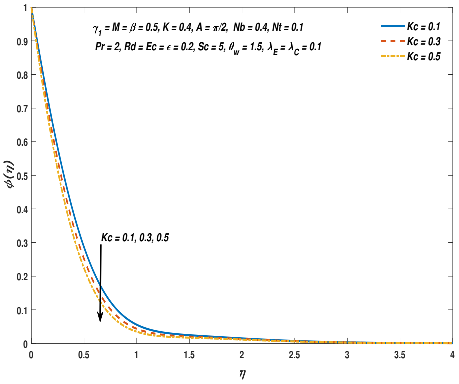

FIGURE 18. Concentration against K_c

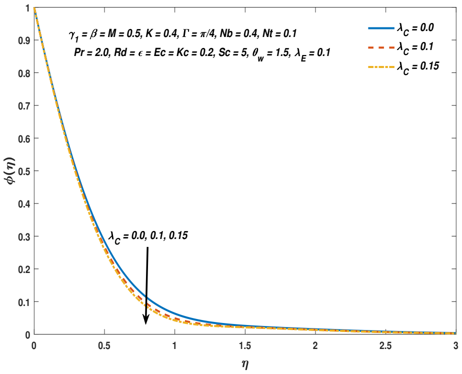

FIGURE 19. Concentration distribution against λ_C

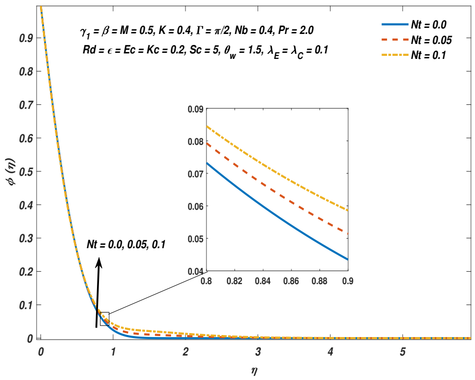

FIGURE 20. Concentration distribution against Nt

- The Sherwood number increases by 0.26% to 0.39% with rising concentration relaxation time and the chemical reaction parameter further boosts the mass transfer due to stronger surface species consumption.

REFERENCES

[1] B. J. Akinbo and B. I. Olajuwon, *Significance of Cattaneo–Christov heat flux model and heat generation/absorption with chemical reaction in Walters' B fluid via a porous medium in the presence of Newtonian heating*, Int. J. Model. Simul., *45* (2025), 137–146.

[2] A. O. Ali, O. D. Makinde, and Y. Nkansah-Gyekye, *Numerical study of unsteady MHD Couette flow and heat transfer of nanofluids in a rotating system with convective cooling*, Int. J. Numer. Methods Heat Fluid Flow, *26* (2016), 1567–1579.

[3] A. M. Alqahtani, K. Rafique, Z. Mahmood, B. R. Al-Sinan, U. Khan, and A. M. Hassan, *MHD rotating flow over a stretching surface: The role of viscosity and aggregation of nanoparticles*, Heliyon, *9* (2023).

[4] K. F. Al Oweidi, W. Jamshed, B. S. Goud, I. Ullah, Usman, M. Isa, M. El Din, K. Guedri, and R. A. Jaleel, *Partial differential equations modeling of thermal transportation in Casson nanofluid flow with Arrhenius activation energy and irreversibility processes*, Sci. Rep., *12* (2022), 20597.

[5] M. Archana, B. J. Gireesha, B. C. Prasannakumara, and R. S. R. Gorla, *Influence of nonlinear thermal radiation on rotating flow of Casson nanofluid*, Nonlinear Eng., *7* (2018), 91–101.

[6] G. Birkhoff, *Numerical fluid dynamics*, SIAM Rev., *25* (1983), 1–34.

[7] A. S. Butt, A. Ali, and A. Mehmood, *Study of flow and heat transfer on a stretching surface in a rotating Casson fluid*, Proc. Natl. Acad. Sci. India Sect. A Phys. Sci., *85* (2015), 421–426.

[8] N. Casson, *Flow equation for pigment-oil suspensions of the printing ink-type*, Rheology Disperse Syst., (1959), 84–104.

[9] C. Cattaneo, *Sulla conduzione del calore*, Atti Sem. Mat. Fis. Univ. Modena, *3* (1948), 83–101.

[10] C. I. Christov, *On frame indifferent formulation of the Maxwell–Cattaneo model of finite-speed heat conduction*, Mech. Res. Commun., *36* (2009), 481–486.

[11] S. Das, R. N. Jana, and O. D. Makinde, *Transient hydromagnetic reactive Couette flow and heat transfer in a rotating frame of reference*, Alexandria Eng. J., *55* (2016), 635–644.

[12] J. B. J. Fourier, *Théorie analytique de la chaleur*, vol. 1, Gauthier-Villars, 1888.

[13] M. Hofer, G. Rappitsch, K. Perktold, W. Trubel, and H. Schima, *Numerical study of wall mechanics and fluid dynamics in end-to-side anastomoses and correlation to intimal hyperplasia*, J. Biomech., *29* (1996), 1297–1308.

[14] T. Hayat, T. Muhammad, A. Alsaedi, and M. S. Alhuthali, *Magnetohydrodynamic three-dimensional flow of viscoelastic nanofluid in the presence of nonlinear thermal radiation*, J. Magn. Magn. Mater., *385* (2015), 222–229.

[15] T. Islam, M. N. Alam, S. Niazai, I. Khan, M. Fayz-Al-Asad, and S. Alqahtani, *Heat generation/absorption effect on natural convective heat transfer in a wavy triangular cavity filled with nanofluid*, Sci. Rep., *13* (2023), 21171.

[16] W. Jamshed, M. Goodarzi, M. Prakash, K. S. Nisar, M. Zakarya, A. H. Abdel-Aty, et al., *Evaluating the unsteady Casson nanofluid over a stretching sheet with solar thermal radiation: An optimal case study*, Case Stud. Therm. Eng., *26* (2021), 101160.

[17] M. D. Kumar, D. Gurram, S. J. Yook, C. S. K. Raju, and N. A. Shah, *Optimizing thermal performance of water-based hybrid nanofluids with magnetic and radiative effects over a spinning disc*, Chemom. Intell. Lab. Syst., *2025*, 105336.

[18] H. Liu, C. P. Ellington, K. Kawachi, C. V. D. Berg, and A. P. Willmott, *A computational fluid dynamic study of hawkmoth hovering*, J. Exp. Biol., *201* (1998), 461–477.

[19] F. Mabood, S. M. Ibrahim, and W. A. Khan, *Framing the features of Brownian motion and thermophoresis on radiative nanofluid flow past a rotating stretching sheet with magnetohydrodynamics*, Results Phys., *6* (2016), 1015–1023.

[20] O. D. Makinde and A. S. Eegunjobi, *Entropy analysis of thermally radiating magnetohydrodynamic slip flow of Casson fluid in a microchannel filled with saturated porous media*, J. Porous Media, *19* (2016).

[21] S. Nadeem, R. Mehmood, and N. S. Akbar, *Oblique stagnation point flow of a Casson nanofluid towards a stretching surface with heat transfer*, J. Comput. Theor. Nanosci., *11* (2014), 1422–1432.

[22] P. F. Neményi, *The main concepts and ideas of fluid dynamics in their historical development*, Arch. Hist. Exact Sci., *2* (1962), 52–86.

[23] B. C. Prasannakumara, B. J. Gireesha, and P. T. Manjunatha, *Melting phenomenon in MHD stagnation point flow of dusty fluid over a stretching sheet in the presence of thermal radiation and non-uniform heat source/sink*, Int. J. Comput. Methods Eng. Sci. Mech., *16* (2015), 265–274.

[24] M. M. Rashidi, S. Abelman, and N. F. Mehr, *Entropy generation in steady MHD flow due to a rotating porous disk in a nanofluid*, Int. J. Heat Mass Transf., *62* (2013), 515–525.

[25] A. Salmi, H. A. Madkhali, B. Ali, M. Nawaz, S. O. Alharbi, and A. S. Alqahtani, *Numerical study of heat and mass transfer enhancement in Prandtl fluid MHD flow using Cattaneo–Christov heat flux theory*, Case Stud. Therm. Eng., *33* (2022), 101949.

[26] M. Senapati, K. Swain, and S. K. Parida, *Numerical analysis of three-dimensional MHD flow of Casson nanofluid past an exponentially stretching sheet*, Karbala Int. J. Mod. Sci., *6* (2020), 13.

[27] H. Shahzad and M. Sagheer, *Forchheimer model and generalized Fourier and Fick heat flux in water based Williamson hybrid nanofluid flow over stretched surface under Lorentz force*, Phys. Scr., *2024*.

[28] B. M. Shankaralingappa, B. C. Prasannakumara, B. J. Gireesha, and I. E. Sarris, *The impact of Cattaneo–Christov double diffusion on Oldroyd-B fluid flow over a stretching sheet with thermophoretic particle deposition and relaxation chemical reaction*, Inventions, *6* (2021), 95.

[29] B. K. Sharma, U. Khanduri, N. K. Mishra, and K. S. Mekheimer, *Combined effect of thermophoresis and Brownian motion on MHD mixed convective flow over an inclined stretching surface with radiation and chemical reaction*, Int. J. Mod. Phys. B, *37* (2023), 2350095.

[30] M. Sheikholeslami and S. A. Shehzad, *Thermal radiation of ferrofluid in existence of Lorentz forces considering variable viscosity*, Int. J. Heat Mass Transf., *109* (2017), 82–92.

[31] M. Sohail, E. R. El-Zahar, A. A. A. Mousa, U. Nazir, S. Althobaiti, A. Althobaiti, N. A. Shah, and J. D. Chung, *Finite element analysis for ternary hybrid nanoparticles on thermal enhancement in pseudo-plastic liquid through porous stretching sheet*, Sci. Rep., *12* (2022), 9219.

[32] A. B. Vishalakshi, U. S. Mahabaleshwar, M. H. Ahmadi, and M. Sharifpur, *An MHD Casson fluid flow past a porous stretching sheet with threshold non-Fourier heat flux model*, Alexandria Eng. J., *69* (2023), 727–737.

[33] C. Y. Wang, *Stretching a surface in a rotating fluid*, Z. Angew. Math. Phys., *39* (1988), 177–185.

[34] K. Zaimi, A. Ishak, and I. Pop, *Stretching surface in rotating viscoelastic fluid*, Appl. Math. Mech., *34* (2013), 945–952.